Lyα Emission from [O III] Emitters Near Reionization: The role of environment in galaxy Lyα detection

Seyedazim Hashemi,[1]★ George D. Becker,[1] Yongda Zhu,[2] Hui Hong[1]
[1]Department of Physics & Astronomy, University of California, Riverside, CA, 92521, USA
[2]Steward Observatory, University of Arizona, 933 N Cherry Ave, Tucson, AZ 85721, USA

arXiv:2507.16231v2 [astro-ph.GA] 30 Jul 2025

Accepted XXX. Received YYY; in original form ZZZ

ABSTRACT

Using galaxy Lyα emission to probe reionization relies on establishing baseline expectations for its detectability in the absence of attenuation by neutral gas in the IGM. Towards this end, the growing numbers of $z \sim 5$–6 star-forming galaxies spectroscopically selected by *JWST* provide an ideal sample for determining how Lyα emission depends on galaxy properties and environment after reionization has largely completed. In this study, we use Keck LRIS to measure the Lyα emission of 46 *JWST*-selected [O III]-emitting galaxies over $5.3 \lesssim z \lesssim 6.2$ in the foreground of the ultra-luminous quasar J0100+2802. Overall, we find that the fraction of galaxies detected in Lyα emission is consistent with previous works; however, the fraction also varies with environment. Most notably, we find an apparent deficit of Lyα in the largest group in our sample, at $z \simeq 6.19$, which falls within the redshift range of the quasar's highly ionized proximity zone. We speculate that the Lyα emission from this group may be partly scattered by a foreground neutral island. In contrast, we detect a high rate of Lyα emission in two groups at $z \simeq 5.73$ and $z \simeq 5.78$. These groups may be part of a structure that is extended along the line of sight, enhancing the transmission of Lyα emission. While our sample size is limited, our results suggest that environment may play a significant role in the detectability of galaxy Lyα emission even as late as $z \sim 6$.

Key words: (cosmology:) dark ages, reionization, first stars – (galaxies:) intergalactic medium – galaxies: high-redshift – (cosmology:) large-scale structure of Universe

1 INTRODUCTION

Over the past two decades a variety of observational tools have put strong constraints on the timing of hydrogen reionization. Measurements of CMB electron scattering optical depth imply a midpoint of reionization near $z \sim 7$–8 (e.g., Planck Collaboration et al. 2020). Damping wing absorption in the spectra of the most distant known quasars also support a large neutral fraction at $z \sim 7$ (e.g., Mortlock et al. 2011; Greig et al. 2017; Bañados et al. 2018; Davies et al. 2018; Greig et al. 2019; Wang et al. 2020; Yang et al. 2020; Greig et al. 2022) that decreases toward $z \sim 6$ (Ďurovčíková et al. 2024; Greig et al. 2024). Recently, damping-wing absorption detected in galaxy spectra with *JWST* has also been used to probe the neutral fraction, supporting a fully neutral IGM at $z \gtrsim 9$ (Umeda et al. 2024, 2025a,b; Mason et al. 2025). Meanwhile, Lyα forest absorption in quasar spectra indicate that while reionization is largely ($\gtrsim$80%) complete by $z \sim 6$, islands of neutral gas may persist in the IGM as late as $z \sim 5.3$ (e.g., Fan et al. 2006; McGreer et al. 2015; Becker et al. 2015; Bosman et al. 2018; Eilers et al. 2018; Yang et al. 2020; Bosman et al. 2022; Zhu et al. 2022, 2024; Spina et al. 2024; Becker et al. 2024). In good agreement with quasar Lyα forest studies, galaxies are also now being used to measure Lyα forest absorption (Meyer et al. 2025).

One of the most important tools for studying reionization is galaxy Lyα emission (e.g., Dijkstra 2014). Strong Lyα emission is frequently observed in galaxies at redshift $z < 6$ (e.g., Stark et al. 2011; Curtis-Lake et al. 2012; Cassata et al. 2015; De Barros et al. 2017; Tang et al. 2024b), but it becomes increasingly more rare at higher redshifts (e.g., Schenker et al. 2012, 2014; Treu et al. 2013; Pentericci et al. 2014, 2018; Tang et al. 2024c; Witstok et al. 2025). The decline is commonly attributed to scattering by neutral hydrogen in the IGM. Measurements of the galaxy Lyα fraction can thus serve as a probe of reionization IGM at higher redshifts than are accessible with Lyα forest absorption, which typically saturates at $z \gtrsim 6$. The global galaxy Lyα fraction can either be directly calculated by measuring the incidence of Lyα emission among galaxies with independent redshift constraints (e.g., Stark et al. 2011; Tang et al. 2024c), or inferred by comparing the Lyα luminosity function of Lyα-selected galaxies (typically from narrow-band or blind spectroscopic surveys) to the UV luminosity function of continuum-selected galaxies (e.g., Ouchi et al. 2010; Santos et al. 2016; Ota et al. 2017; Konno et al. 2018; Runnholm et al. 2025). Both methods indicate a decline in the fraction of galaxies with detectable Lyα and a corresponding increase in the IGM neutral fraction that rises rapidly at $z > 6$ (e.g., Schenker et al. 2012; Treu et al. 2013; Pentericci et al. 2014, 2018; Mason et al. 2018a, 2019; Whitler et al. 2020; Bolan et al. 2022; Goto et al. 2021; Tang et al. 2024c; Kageura et al. 2025). In addition to

★ E-mail: seyedazim.hashemi@email.ucr.edu

© 2025 The Authors

providing global constraints on the IGM, galaxy Lyα emission can be used to trace the growth of individual ionized bubbles (e.g., Barkana & Loeb 2004; Furlanetto et al. 2004; Wyithe & Loeb 2005; Iliev et al. 2006; Dayal & Ferrara 2018; Weinberger et al. 2018; Endsley et al. 2021; Trapp et al. 2023; Hayes & Scarlata 2023; Lu et al. 2025).

Multiple factors can impact the detectability of galaxy Lyα. For example, galaxy gas dynamics may play a role. If most of the Lyα photons from a galaxy are already significantly redshifted from their systematic redshift, its Lyα emission can pass through the IGM even if the galaxy is located in a small ionized region (e.g., Erb et al. 2014; Willott et al. 2015; Mason et al. 2018b; Hashimoto et al. 2019; Matthee et al. 2020; Endsley et al. 2022). Furthermore, some galaxies may have an intense radiation field the facilitates the production and visibility of Lyα from small ionized bubbles (e.g., Stark et al. 2017; Endsley et al. 2021; Simmonds et al. 2023; Tang et al. 2023; Roberts-Borsani et al. 2023). Recently, several studies have data from the *James Webb Space Telescope* (*JWST*) to investigate conditions favorable for detecting LAEs. In addition to being located within large ionized bubbles (e.g., Witten et al. 2024; Witstok et al. 2024; Chen et al. 2024; Whitler et al. 2024), Witten et al. (2024) suggested that galaxy mergers, which generate a significant number of Lyα photons, along with a 'favorable' line-of-sight—cleared of local neutral hydrogen in the host galaxy—are key factors in making Lyα emission detectable. The line-of-sight extension of galaxy groups has also been proposed as a potential factor in Lyα detection (Chen et al. 2024).

Increasing the robustness of galaxy Lyα emission as a tracer of reionization requires establishing a robust baseline for the detectability of Lyα in the absence of scattering by a neutral IGM. In order to minimize the impact of galaxy evolution, this baseline should be set soon after reionization ends. An ideal sample would include galaxies in a range of environments with secure spectroscopic redshifts measured independently from Lyα. Fortunately, several *JWST* programs are now providing such samples. Surveys such as EIGER and ASPIRE are identifying large samples of [O III]-selected galaxies at $z \lesssim 6$ via NIRCam wide-field slitless spectroscopy (e.g., Kashino et al. 2023; Matthee et al. 2023; Eilers et al. 2024; Wang et al. 2023). Because the surveys are conducted in the fields of background quasars, they also provide the opportunity to examine the connections between galaxies and the IGM properties traced by the quasar spectra (e.g., Kashino et al. 2023; Jin et al. 2024; Kakiichi et al. 2025; Conaboy et al. 2025).

In this paper we present a pilot study of the connection between Lyα detectability and environment in [O III]-selected galaxies at $z \lesssim 6$. We use Keck LRIS to measure Lyα the emission from a sample of galaxies identified in the EIGER survey by Kashino et al. (2023). The galaxies span a range of environment, from isolated to large groups. Although our sample is relatively small, we find tentative evidence that environment may indeed play a role in Lyα detectability even near the end of reionization.

The organization of the remainder of the paper is as follows. In Section 2, we describe our sample of [O III]-selected galaxies, LRIS observations and data reduction. In Section 3, we examine the Lyα equivalent width (W) distribution and its variation among the groups in our sample. We find that a large group at $z = 6.19$ appears to show significantly less Lyα than the remainder of the sample, and discuss possible explanations. We also find that a two smaller groups at $z \simeq 5.7$–5.8 that are aligned along the line of sight exhibit a possible Lyα enhancement. Finally, we summarize our results and conclusions in Section 4. In this work, we assume a flat ΛCDM cosmology with $H_0 = 67.4$ km s^{-1} Mpc^{-1} and $\Omega_M = 0.315$ (Planck Collaboration et al. 2020). All magnitudes are quoted in the AB system Oke & Gunn (1983), and emission line equivalent widths are measured in the rest frame.

2 Lyα MEASUREMENTS

2.1 Target selection

Our targets are drawn from the sample of [O III]-emitting galaxies in the field of SDSS J010013.02+280225.8 (hereafter J0100+2802) identified in the EIGER survey (JWST Program ID GO-1243, PI: Lilly). EIGER uses JWST NIRCam imaging and wide-field slitless spectroscopy to identify line-emitting galaxies in the fields of six $z > 6$ quasars. For [O III] emission, the wavelength coverage spans $5.3 \lesssim z \lesssim 7$. The footprint is approximately 6.5×3.4 arcmin^2, or up to ~10 cMpc/h around the sight line. Kashino et al. (2023) identify 117 [O III]-emitting systems within this window towards J0100+2802. These galaxies span a wide range in UV ($-22.3 \leq M_{\rm UV} \leq -17.7$) and [O III] luminosity ($41.8 \leq \log_{10}(L_{\rm [O\,III]}/{\rm erg\ s^{-1}}) \leq 43.4$). The sample includes three prominent overdensities. One of these is situated behind the quasar, at $z \simeq 6.78$. The second includes J0100+2802 itself, while the third occurs at $z \simeq 6.19$, which coincides in redshift with the end of the quasar's proximity zone. As argued by Matthee et al. (2023), the narrow [O III] line widths and extended morphologies suggest that the emission of these sources is typically powered by star formation.

In this work we target 46 galaxies in the foreground of J0100+2802. The galaxies were chosen to span a range of environments and redshifts and also are prioritized based on the confidence of their [O III] detections. We also attempted to optimize the number of galaxies that could be observed using only two masks in order to increase the exposure time for each object. The spatial distribution of these galaxies relative to the central quasar is shown in Figure 1. Distributions of redshift, [O III] luminosity, and $M_{\rm UV}$ are presented in Figure 2. The $L_{\rm [O\,III]}$ and $M_{\rm UV}$ values of our targets span nearly the full range of the EIGER sample. Based on their spatial distribution and similarity in redshift ($\Delta z < 0.02$), we identify six galaxy groups among our targets (see Figure 1). Notably, our sample includes 15 objects from the large overdensity at $z \simeq 6.19$. We return to this overdensity below.

2.2 Keck LRIS data

We observed our objects with Keck LRIS over two half-nights on November 12 (Night 1) and 13 (Night 2) in 2023. The observations were conducted using the 600/10000 grating on the red side with the 560 nm dichroic, and 1.0″ slit width. We also obtained blue-side spectra with the 600/4000 grism, although those data are not used in this work. The average seeing was ~0.6″ on the first night and ~ 1.0″ on the second night. The targets were divided roughly equally between two masks. For each mask we obtained 18 exposures of 900s each, giving a total exposure time of 4.5 hours.

The data were reduced using a custom software package developed for faint-object spectroscopy. Individual exposures were flat-fielded and optimally sky-subtracted in the un-rectified frame following Kelson (2003). A combination of alignment star traces and slit edges was used to compute a spatial solution for each exposure. A single rectified two-dimensional spectrum for each object was then extracted simultaneously from all exposures. Finally, we extracted one-dimensional spectra from the combined 2D spectra using boxcar extraction. The spatial aperture size used for extraction was 2.025 arcseconds, which was larger than the typical seeing.

For some objects we noted small zero-point offsets (up to ~ 2 ×

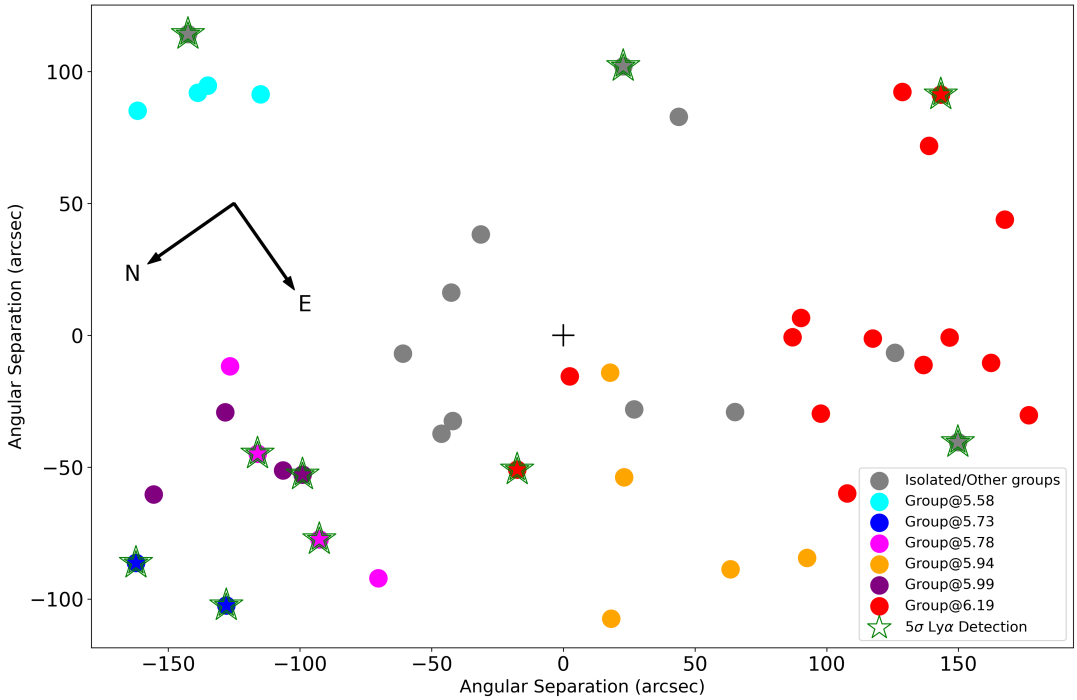

Figure 1. Spatial distribution of [O III] emitters in the field of J0100+2802 targeted with Keck LRIS. Colors indicate membership in the groups listed in the legend. Gray points represent galaxies that are not part of any group in our sample; however, they may belong to a group in the parent [O III] sample. The black cross at the center marks the position of the quasar. Green stars denote sources where we detect Lyα emission at more than 5σ confidence. Orientation is chosen to be similar to Figure 7 in Kashino et al. 2023.

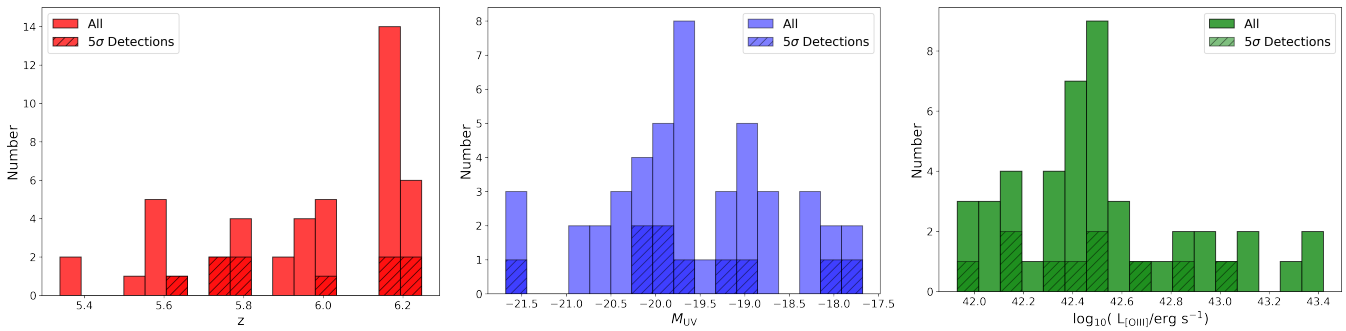

Figure 2. Distribution of redshift (left), $M_{\rm UV}$ (center) and [O III] luminosity (right) of the galaxies in our sample. Sources with Lyα detected at $>5\sigma$ confidence are indicated with a hatched pattern.

10^{-20} erg cm^{-2} s^{-1} Å^{-1}) in the 1D spectra over extended regions blueward of Lyα, which we attribute to small errors in sky subtraction or contamination from foreground continuum objects. To correct for these effects, we measured the median flux within a one arcsecond window spanning -2000 km s^{-1} to -500 km s^{-1} (i.e., blueward) of Lyα at the systematic redshift of the object, and subtracted it from the 2D spectrum over all wavelengths before re-extracting the 1D spectrum. In some cases this procedure also helped remove obvious continuum flux from foreground objects (e.g., ID 13503; Figure A2).

We found that our formal error estimates closely reflected the pixel-to-pixel scatter in the 1D spectrum except over wavelengths affected by strong sky emission lines. We remedied this by increasing the errors in skyline regions using the following procedure. We first measured the minimum error within ± 2000 km s^{-1} of Lyα at the systematic redshift. The excess error above this minimum was then increased by a factor of two for all pixels. This procedure effectively increases the errors around skylines by a factor of two while leaving the error at other wavelengths relatively unchanged.

A representative sample of our LRIS spectra is shown in Figure 3. The remainder are included in Appendix A1. Lyα line fluxes were measured by integrating the 1D spectra in a window from 0 to 500 km s^{-1} redward of the systematic redshift measured from [O III]. The choice of window is motivated by the maximum velocity extent of Lyα seen in individual objects (e.g., ID 5955 and ID 1233) and the apparent absence of blue peaks. The Lyα line fluxes are corrected for the underlying continuum using estimates derived from NIRCam *JWST* F115W and F200W photometry (Kashino et al. 2023). A power-law continuum of the form $f_\lambda \propto \lambda^\beta$ was fit to the photometry, and subtracted from the observed Lyα fluxes. The Lyα measurements are summarized in Table 1. Our median 5σ sensitivity is 2.9×10^{-17} erg s^{-1} cm^{-2} over $5.3 < z < 6.3$; however, residuals from strong skylines significantly decrease our sensitivity for some objects, as

reflected in the flux uncertainties. We note that Lyα measurements are not corrected for slit losses.

In total, we detect Lyα emission in 10 (17) galaxies out of 46 with at least 5σ (3σ) confidence. The spatial and redshift distribution of the detections is illustrated in Figure 4. As shown below, our overall detection rate is consistent with other recent searches for Lyα from [O III]-selected galaxies (Tang et al. 2024a). We note, however, that our detection rate varies significantly between groups. Some of this is due to observational effects. For example, our sensitivity to Lyα is lower for the $z \simeq 5.58$ and $z \simeq 5.99$ groups due to strong skyline residuals. Redshifts with strong skyline residuals (corresponding to wavelengths where the LRIS flux errors are greater than 1.4 times the median) are shown in the lower panel of Figure 4. There are three cases, however, for which the fraction of detected Lyα seems to differ significantly from the mean. The group of five galaxies at $z \simeq 5.94$ show effectively Lyα emission. This is a small group for which the lack of Lyα may be a statistical fluctuation. The Lyα fraction also appears to be unusually low, however, in the larger group of 15 galaxies at $z \simeq 6.19$. Finally, our detection rate is notably *higher* than average in the pair of smaller groups at $z \simeq 5.73$ and 5.78. Our main focus of this paper is the $z \simeq 6.19$ group, but we return to the objects at $z \simeq 5.73$–5.78 in Section 3.3.

3 RESULTS

3.1 Global Lyα equivalent width distribution

We first examine the global properties of Lyα emission in our sample, then turn to variations between groups below. We convert our Lyα flux measurements to equivalent widths using continuum estimates derived from photometry (see Section 2.2 for more detail). The W values are computed by dividing the measured Lyα line fluxes by the continuum flux density determined from the power law at 1216 Å. Errors in the equivalent widths are computed using a Monte Carlo approach that includes both uncertainties in the Lyα fluxes and uncertainties in the *JWST* fluxes. The results are summarized in Table 1.

For the W distribution, we apply a Bayesian framework and assume a log-normal distribution to construct the Lyα W distributions. This distribution is characterized by a set of parameters $\theta = [\mu, \sigma]$, where μ and σ are the mean and standard deviation, respectively, of $\ln W$. We use uniform priors for the model parameters, with μ ranging from 0 to 6 and σ ranging from 0.01 to 4 (see also Schenker et al. 2014; Endsley et al. 2021; Tang et al. 2024a).

For each set of model parameters θ, the log-normal distribution is

$$p(W|\theta) = \frac{1}{\sqrt{2\pi}\,\sigma W} \exp\left[-\frac{(\ln W - \mu)^2}{2\sigma^2}\right]. \quad (1)$$

We compute a likelihood for each galaxy by convolving the model distribution with $p_{\mathrm{obs},i}(W)$, the full empirical (and typically non-Gaussian) probability distribution of W for galaxy i,

$$p(\mathrm{obs}, i|\theta) = \int_{-\infty}^{\infty} p_{\mathrm{obs},i}(W)\, p(W|\theta)\, dW\,. \quad (2)$$

The likelihood for the entire sample is then determined by multiplying the individual likelihoods for each galaxy,

$$p(\mathrm{obs}|\theta) \propto \prod_i p(\mathrm{obs}, i|\theta). \quad (3)$$

Using Bayes' theorem, we express the posterior probability distribution for the model parameters as $p(\theta|\mathrm{obs}) \propto p(\theta)p(\mathrm{obs}|\theta)$, where $p(\theta)$ represents the prior of the model parameters. We first apply the model to the full sample. The result shown on the left side of Figure 7 is consistent with a recent study by Tang et al. (2024a). As discussed below, however, the Lyα properties of individual groups may differ significantly from one another.

3.2 A large group with a significant Lyα deficit?

The group of 15 galaxies at $z \simeq 6.19$ is the largest group in our sample. This structure is located $\sim$38 h^{-1} cMpc in the foreground of the J0100, corresponding in redshift to the end of the quasar's proximity zone (Kashino et al. 2023). Given that the IGM within the proximity zone must be highly ionized, we might expect that the observed Lyα fraction for this group would be equal to or greater than the global average. Notably, however, we have detected Lyα emission from only two (five) sources at 5σ (3σ) confidence. We also note that the two detected LAEs are also located at the edges of the group, with one very close to the quasar line of sight. We return to this point below.

We note that our Lyα measurements for the $z \simeq 6.19$ group are not impacted by strong skylines. Furthermore, the distribution of UV magnitudes and [O III] luminosity of galaxies in this group are broadly consistent with the rest of the sample (see Figure 5). We also calculated the mean UV slope for this group (-1.69 ± 0.11) and the rest of the sample (-1.79 ± 0.17) using two filters (F115W and F200W) and found that they are consistent within the 1σ errors. This suggests that the dust content of the $z \simeq 6.19$ galaxies is not obviously different from the rest of the sample. If the observed Lyα emission from this group is significantly lower than the remainder of the sample, therefore, it is possible that its Lyα emission is attenuated by intervening gas.

In order to determine whether the apparent deficit in the $z \simeq 6.19$ group is significant, we compare this group to the rest of the sample using two quantities, the rest-frame Lyα equivalent width (W) distribution, and the ratio of Lyα and [O III] Luminosities. As a visual demonstration, we compare the stacked spectra of the $z \simeq 6.19$ group to that of the rest of the sample in Figure 6. To exclude pixels affected by strong sky lines, we exclude regions from individual spectra where the corresponding flux uncertainty exceeds 1.4 times the median of the full error array for that spectrum. In the left-hand plot, we normalize each individual spectrum by its [O III] luminosity, while in the right-hand plot, they are normalized by their UV luminosities. In both cases the mean Lyα emission in the $z \simeq 6.19$ group is roughly a factor of three lower than the mean of the other sources.

In order to better quantify this apparent difference, we first compare the Lyα equivalent width distribution of the $z \simeq 6.19$ group to that of the rest of the sample. We apply the fitting formalism described above to these subsamples separately, with results presented on the right-hand side of Figure 7. There is some evidence that the best-fitting lognormal parameters differ; however, the parameters for the $z \simeq 6.19$ group are poorly constrained due to the small sample size and overlap significantly with those for the rest of the sample. We note that the result does not strongly depend on the choice of the underlying W distribution model; adopting an exponential functional $p(W) \propto \exp(-W/W_0)$, yields similar conclusions. As a related test, we adopt the lognormal parameters for the rest of the sample as the parent distribution and calculate the probability that a group of 15 galaxies would randomly have a mean equivalent width as low as the one observed for the $z \simeq 6.19$ group. For this test, we randomly draw parameters from the distribution shown in Figure 7 in a probability-weighted way, and then generate a random sample of 15 W values for each set of parameters. The randomly generated groups have a mean W that exceeds the $z \simeq 6.19$ value in 70% of the trials. This suggests

ID	RA deg	Dec deg	$z_{\rm spec}$	$M_{\rm UV}$ (mag) (mag)	$\log_{10}(L_{[\rm O\,III]}/{\rm erg\,s^{-1}})$	Lyα Flux $\times10^{-18}$ erg cm^{-2} s^{-1}	W (Lyα) Å	Note
5891	15.0554	28.0570	5.338	-20.32 ± 0.20	42.45 ± 0.08	7.4 ± 6.7	$25.8^{+27.3}_{-23.3}$	—-
9327	15.0758	28.0129	5.363	-18.27 ± 0.15	42.10 ± 0.12	5.6 ± 3.0	$244.5^{+201.1}_{-136.7}$	—-
6228	15.0550	28.0552	5.508	-19.67 ± 0.16	41.96 ± 0.14	1.0 ± 8.9	$10.8^{+97.4}_{-95.8}$	—-
8768	15.0461	28.0555	5.570	-19.77 ± 0.07	42.14 ± 0.07	10.1 ± 6.9	$47.3^{+33.0}_{-32.2}$	—-
12083	15.0151	28.0521	5.573	-19.88 ± 0.09	42.47 ± 0.05	-2.9 ± 6.4	$-15.1^{+32.9}_{-33.5}$	Group@5.58
12410	15.0112	28.0561	5.575	-19.04 ± 0.19	42.46 ± 0.07	12.3 ± 6.8	$123.2^{+88.5}_{-69.5}$	Group@5.58
12314	15.0112	28.0574	5.575	-20.67 ± 0.08	43.15 ± 0.02	0.0 ± 6.5	$0.1^{+16.8}_{-17.0}$	Group@5.58
12919	15.0091	28.0637	5.579	-18.78 ± 0.21	42.07 ± 0.12	3.7 ± 3.7	$61.3^{+78.3}_{-61.7}$	Group@5.58
5955	15.0873	28.0129	5.659	-19.84 ± 0.12	42.65 ± 0.04	65.2 ± 2.7	$303.2^{+45.9}_{-37.8}$	—-
1233	15.0480	28.0911	5.718	-17.97 ± 0.38	42.17 ± 0.11	16.9 ± 2.0	$346.6^{+314.5}_{-134.4}$	Group@5.73
82	15.0572	28.0859	5.736	-19.15 ± 0.26	42.34 ± 0.09	15.4 ± 2.1	$118.8^{+64.6}_{-36.5}$	Group@5.73
8005	15.0368	28.0712	5.772	-18.63 ± 0.15	42.13 ± 0.05	6.7 ± 2.0	$105.2^{+42.8}_{-34.7}$	Group@5.78
982	15.0640	28.0711	5.775	-19.65 ± 0.09	42.42 ± 0.05	8.1 ± 2.1	$55.3^{+16.2}_{-15.0}$	Group@5.78
5052	15.0460	28.0741	5.777	-20.23 ± 0.11	42.42 ± 0.08	18.2 ± 2.1	$72.7^{+15.1}_{-12.4}$	Group@5.78
2285	15.0571	28.0739	5.777	-21.57 ± 0.05	43.03 ± 0.04	19.4 ± 2.2	$23.1^{+2.9}_{-2.8}$	Group@5.78
19002	15.0438	28.0476	5.908	-18.75 ± 0.11	41.93 ± 0.08	9.7 ± 8.1	$174.0^{+154.3}_{-144.5}$	—-
1591	15.0846	28.0402	5.925	-19.23 ± 0.17	42.37 ± 0.09	-7.7 ± 8.2	$-254.8^{+268.8}_{-491.8}$	Group@5.94
2035	15.0882	28.0329	5.928	-19.77 ± 0.13	42.59 ± 0.04	-4.2 ± 8.3	$-25.6^{+50.7}_{-52.4}$	Group@5.94
4634	15.0702	28.0438	5.942	-19.79 ± 0.11	42.74 ± 0.04	5.7 ± 3.5	$43.7^{+28.6}_{-26.2}$	Group@5.94
8200	15.0603	28.0387	5.943	-18.12 ± 0.14	42.49 ± 0.03	4.4 ± 4.2	$189.2^{+209.6}_{-180.1}$	Group@5.94
31	15.0816	28.0535	5.944	-20.95 ± 0.07	43.26 ± 0.06	-4.0 ± 4.4	$-10.5^{+11.6}_{-11.7}$	Group@5.94
4741	15.04895	28.0729	5.987	-21.56 ± 0.07	43.11 ± 0.02	-10.1 ± 5.7	$-16.4^{+9.3}_{-9.4}$	Group@5.99
6343	15.0404	28.0743	5.987	-19.09 ± 0.15	42.53 ± 0.08	6.0 ± 5.7	$69.0^{+71.7}_{-65.7}$	Group@5.99
3618	15.0432	28.0855	5.990	-20.78 ± 0.08	42.48 ± 0.08	16.6 ± 5.3	$42.1^{+14.6}_{-13.8}$	Group@5.99
4396	15.0505	28.0714	5.990	-20.13 ± 0.07	42.51 ± 0.04	58.5 ± 5.3	$236.9^{+27.7}_{-25.8}$	Group@5.99
6898	15.0649	28.0388	6.014	-20.17 ± 0.12	42.41 ± 0.06	7.7 ± 2.4	$43.6^{+19.1}_{-14.8}$	—-
13635	15.0600	27.9975	6.175	-18.99 ± 0.18	42.56 ± 0.04	2.8 ± 2.0	$40.5^{+35.0}_{-28.6}$	Group@6.19
9209	15.0825	28.0052	6.177	-21.68 ± 0.07	43.42 ± 0.04	-3.9 ± 2.0	$-5.2^{+2.7}_{-2.8}$	Group@6.19
7038	15.0893	28.0051	6.179	-20.02 ± 0.14	42.35 ± 0.07	10.2 ± 2.1	$65.1^{+22.0}_{-16.7}$	Group@6.19
10225	15.0778	28.0072	6.179	-20.03 ± 0.12	43.36 ± 0.06	0.2 ± 2.1	$1.6^{+15.3}_{-15.3}$	Group@6.19
19597	15.0671	28.0189	6.182	-18.37 ± 0.09	42.26 ± 0.07	3.4 ± 2.1	$78.0^{+53.2}_{-48.4}$	Group@6.19
4304	15.0851	28.0255	6.183	-20.49 ± 0.08	42.90 ± 0.03	-1.0 ± 2.2	$-4.6^{+10.1}_{-10.0}$	Group@6.19
10020	15.0732	28.0139	6.184	-19.70 ± 0.11	42.47 ± 0.04	6.9 ± 2.1	$64.5^{+24.1}_{-20.6}$	Group@6.19
13503	15.0766	28.0230	6.184	-20.33 ± 0.15	42.37 ± 0.06	2.1 ± 2.1	$8.8^{+10.9}_{-9.1}$	Group@6.19
11496	15.0563	27.9933	6.185	-20.01 ± 0.14	42.83 ± 0.05	29.4 ± 2.1	$174.0^{+49.3}_{-34.3}$	Group@6.19
11989	15.0538	27.9965	6.186	-19.12 ± 0.32	42.54 ± 0.08	0.7 ± 2.1	$8.2^{+97.0}_{-45.7}$	Group@6.19
4738	15.0630	28.0526	6.187	-19.04 ± 0.11	42.47 ± 0.04	20.9 ± 2.2	$330.4^{+67.3}_{-54.4}$	Group@6.19

Table 1. Information and Lyα properties of observed galaxies. IDs, spectroscopic redshifts, $M_{\rm UV}$, and $\log_{10}(L_{[\rm O\,III]}/{\rm erg\,s^{-1}})$ are from Kashino et al. (2023) and Matthee et al. (2023). Using photometry data from Matthee et al. (2023) to estimate the continuum flux density, we report the median and marginalized 68 percent confidence intervals for the Lyα W.

ID	RA	Dec	$z_{\rm spec}$	$M_{\rm UV}$ (mag)	$\log_{10}(L_{[\rm O\,III]}/{\rm erg\,s^{-1}})$	Lyα Flux	W (Lyα)	Note
	deg	deg		(mag)		$\times10^{-18}$ erg cm^{-2} s^{-1}	Å	
10146	15.0683	28.0208	6.187	-20.69 ± 0.08	42.96 ± 0.11	7.8 ± 2.1	$26.8^{+7.9}_{-7.5}$	Group@6.19
7979	15.0582	28.0424	6.188	-19.53 ± 0.11	42.39 ± 0.05	-1.3 ± 2.1	$-10.3^{+17.7}_{-18.3}$	Group@6.19
8913	15.0786	28.0112	6.193	-19.74 ± 0.17	42.61 ± 0.10	6.4 ± 2.8	$49.9^{+31.0}_{-23.3}$	Group@6.19
16346	15.0710	27.9953	6.194	-20.07 ± 0.15	42.89 ± 0.04	2.3 ± 3.3	$15.9^{+26.1}_{-23.2}$	Group@6.19
12821	15.0424	28.0173	6.203	-19.01 ± 0.22	42.29 ± 0.08	19.0 ± 9.9	$141.9^{+99.3}_{-78.0}$	—
16842	15.0406	28.0415	6.206	-17.83 ± 0.28	42.29 ± 0.04	-6.1 ± 9.5	$-167.8^{+265.8}_{-320.3}$	—
6761	15.0712	28.0303	6.229	-18.30 ± 0.17	42.09 ± 0.07	-2.3 ± 4.5	$-54.4^{+104.4}_{-111.6}$	—
20317	15.0056	28.0547	6.240	-19.66 ± 0.18	42.19 ± 0.11	25.4 ± 2.1	$171.7^{+69.6}_{-43.0}$	—
11016	15.0347	28.0190	6.247	-17.68 ± 0.36	41.97 ± 0.08	13.5 ± 2.3	$472.3^{+421.1}_{-182.3}$	—

Table 1 – *continued*

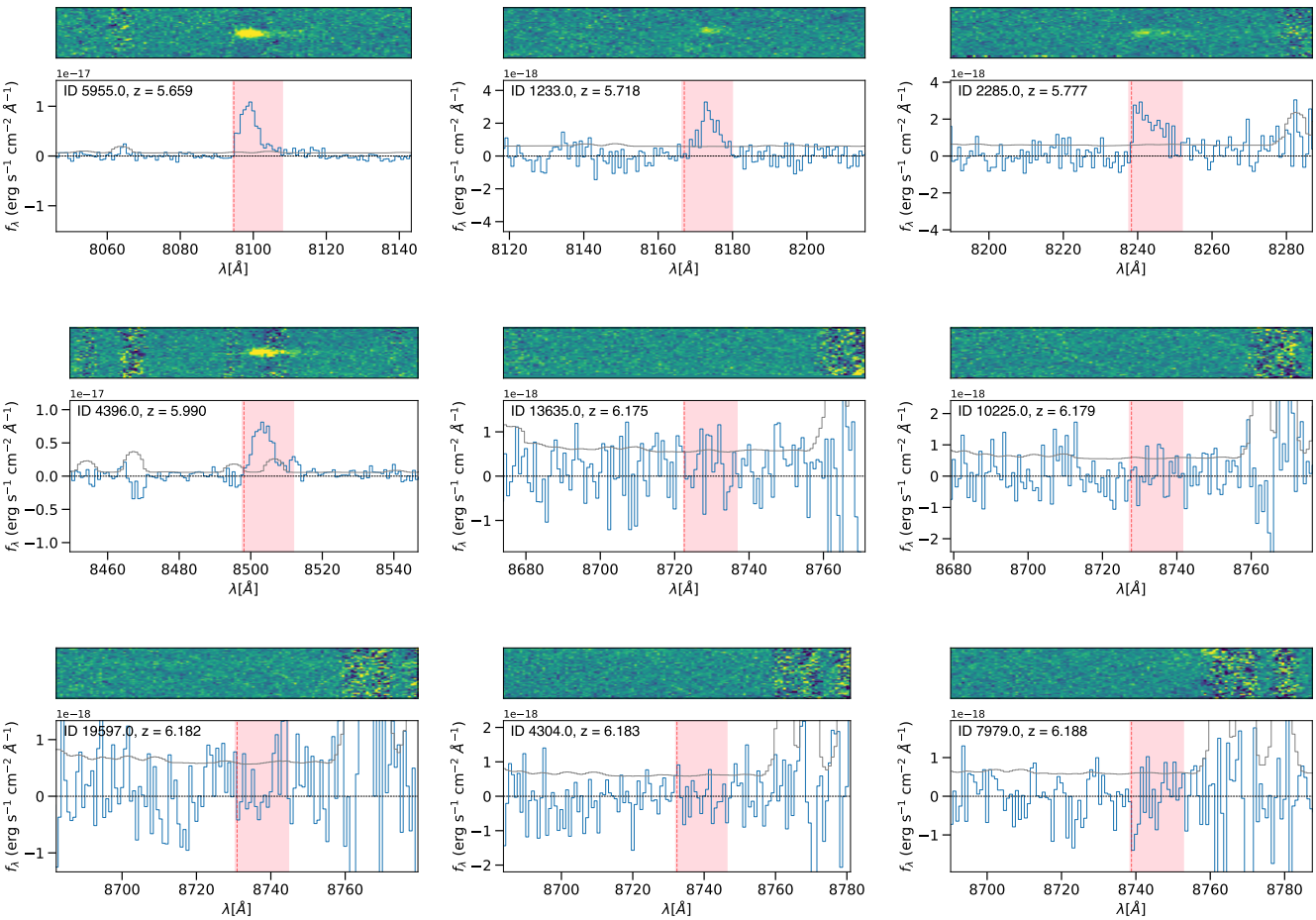

Figure 3. 1D and 2D emission-line spectra of a representative sample of observed galaxies. Each panel is centered on the systematic redshift of the galaxy measured from [O III] (red dashed vertical line). We show the 2D spectrum for each galaxy at the top of each panel. The 1D spectrum (blue histogram) of each emitter in the observed frame is also shown. The uncertainty of the 1D spectrum is plotted in each grey. Shaded regions indicate the 500 km s^{-1} windows used to measure Lyα fluxes. Spectra for the reminder of our objects are shown in figure A1.

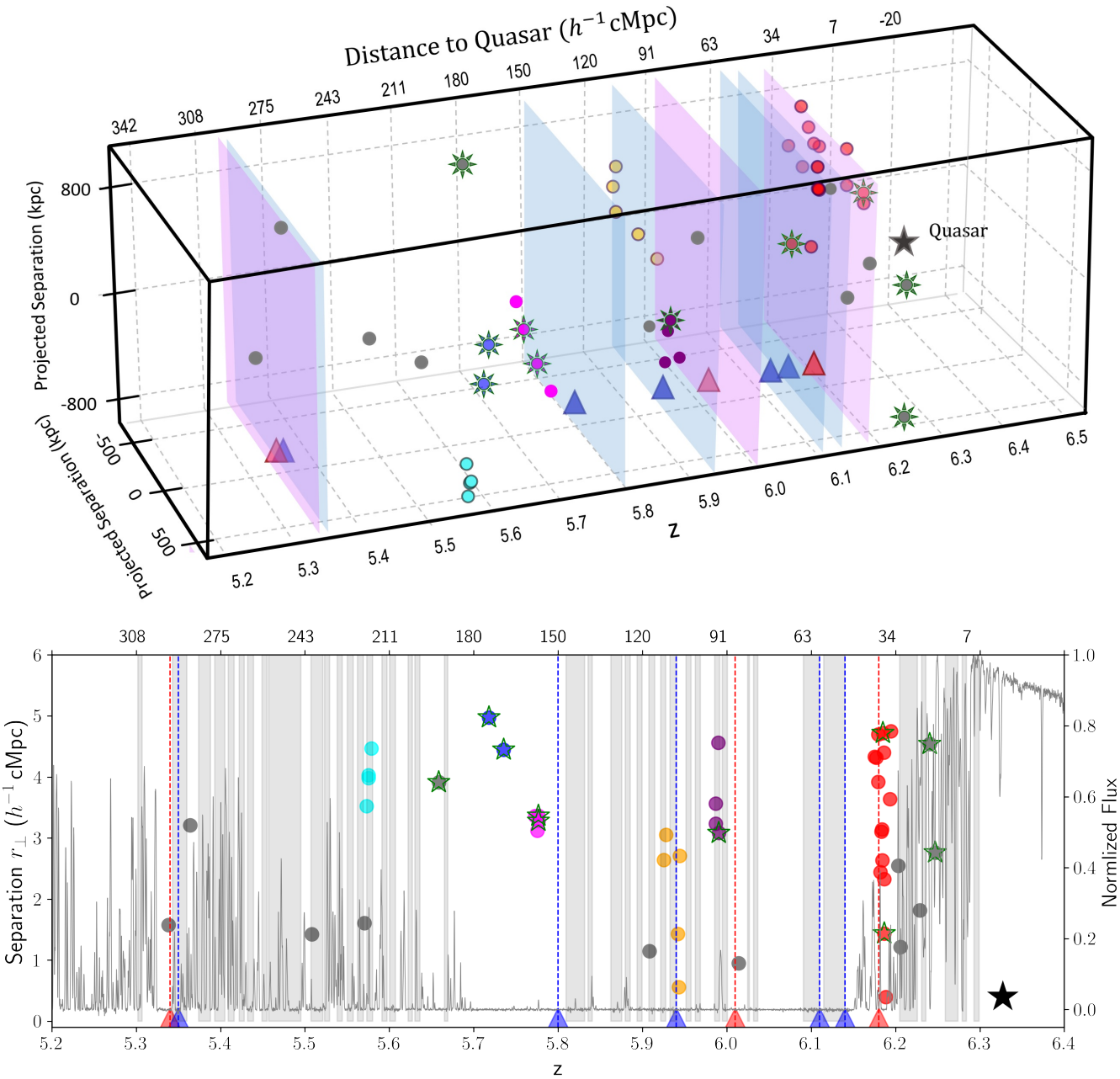

Figure 4. Illustrations of our sample in two viewing angles. Circles show our targeted galaxies, with colors correposnding to Figure 1. A green star means that the galaxy is detected in Lyα at $>5\sigma$ confidence. The black star at the end of the box shows the quasar redshift. Upper axes in both figures show the co-moving distance to the quasar. A blue (red) triangle, extended by a light blue (pink) plane, indicates the redshift of a low-ionization (high-ionization) metal line absorber identified in the spectra of the quasar. Shaded parts in the lower panel show regions affected by sky lines.

that the $z \simeq 6.19$ group may have a significantly lower mean W than the remainder of the sample, through the evidence from this test is weak.

Stronger evidence comes from examining the ratio of Lyα and [O III] luminosities. In principle, intrinsic Lyα emission should be strongly correlated with [O III] as both are tracers of star formation. Figure 8 presents the distribution of $L_{\mathrm{Ly}\alpha}/L_{[\mathrm{O\,III}]}$ for both the 15 galaxies at $z \simeq 6.19$ and the remaining 31 galaxies at other redshifts. The other objects include a tail at $L_{\mathrm{Ly}\alpha}/L_{[\mathrm{O\,III}]} > 4$ that is not present at $z \simeq 6.19$. The mean values are $0.71^{+0.28}_{-0.25}$ at $z \simeq 6.19$ and $1.85^{+0.76}_{-0.69}$ for the remainder. Here, the 68% confidence intervals were computed via bootstrap resampling, with the bootstrap draws taken from the full error distribution for each input Lyα and [O III] measurement. It is not clear from Figure 8 what the underlying functional form of the $L_{\mathrm{Ly}\alpha}/L_{[\mathrm{O\,III}]}$ distribution should be. Nevertheless, we can perform an empirical test of whether the two distributions are consistent with one another. For this we adopt our 31 measurements of $L_{\mathrm{Ly}\alpha}/L_{[\mathrm{O\,III}]}$ outside of the $z \simeq 6.19$ group as our parent distribution, and ask what the probability is of drawing a random set of 15 values from this distribution with a mean value as low as observed at $z \simeq 6.19$. Here again, individual values are drawn from the full error distribution for each measurement. We find that a random sam-

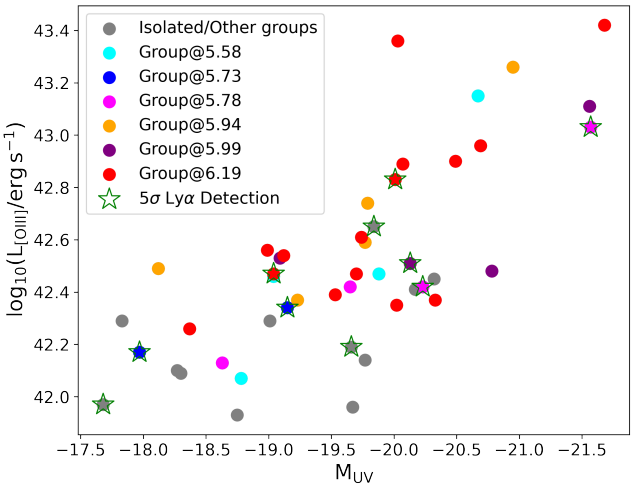

Figure 5. [O III] luminosity vs. UV magnitude for the sources in this study. Groups are color-coded as in Figure 1. Stars indicate sources with 5σ Lyα detections.

ple has a lower mean in only 6% of the trials. While the evidence is still modest, therefore, the ratios of Lyα and [O III] provide some evidence that the mean Lyα emission measured in the $z \simeq 6.19$ group is significantly lower than that of the rest of the sample.

3.2.1 Possible causes of the Lyα deficit

The comparisons above provide some indication that Lyα emission from the large group of [O III] emitters at $z \simeq 6.19$ may be attenuated compared to the rest of the sample. While these test provide only marginal evidence based on the ensemble Lyα properties, the spatial distribution of Lyα in this group is also notable. Specifically, the two galaxies with Lyα detected at $>5\sigma$ confidence lie at the edges of the structure (Figure 1). One of these, moreover, lies within 50 arcseconds (1.4 h^{-1} cMpc) of the quasar line sight, and hence, given its redshift, is very likely to lie within the quasar proximity zone even if the quasar ionizing emission is beamed within a cone of $\lesssim$2 degrees. The fact that there is very little detectable Lyα from within the interior of this group (galaxies 7038, 10020, and 10146 are detected at only 3σ significance) is further reason to suspect that there may be Lyα attenuation over at least part of the structure.

We emphasize that the galaxies in the $z \simeq 6.19$ group have UV magnitudes, [O III] luminosities, and UV slopes that are broadly consistent with the full sample (see Figure 5 and Section 3.2). Still, the galaxies in this group are on average slightly brighter (Figure 5). We therefore conducted an additional test by restricting the full sample to galaxies with $M_{\rm UV} < -19$ and recreating the comparisons shown in Figure 6. This analysis produced no significant change in the results, suggesting that even when compared to similarly bright galaxies, those in the group show more attenuated Lyα emission. We also performed a Mann–Whitney U test comparing the [O III] equivalent widths and UV magnitudes between the $z \simeq 6.19$ group and the rest of the sample. The resulting p-values are 0.54 for [O III] equivalent widths and 0.24 for UV magnitude, confirming that there are no statistically significant differences in these properties.

Another useful quantity for comparing the galaxies in these two samples is the Lyα velocity offset, which can be sensitive to the galaxies' neutral gas content and/or kinematics. Among our 5σ detections, the average Lyα peak velocity offset (measured from the brightest pixel) for the $z \simeq 6.19$ group is ~ 139 km s^{-1}, compared to ~ 180 km s^{-1} for the rest of the sample. A more robust constraint comes from the velocity offset measured in the stacked spectra, which shows no significant difference in the Lyα shift relative to the systemic redshift between the two samples.

If Lyα from this group is unusually weak, it therefore suggests that there may be scattering due to damping wing absorption from intervening neutral hydrogen. Heintz et al. (2024) presented evidence that a proto-cluster at a redshift of $z = 5.4$ may contain a significant amount of neutral gas based on damping absorption measured in background galaxies. While the $z \simeq 6.19$ could potentially also host neutral gas, we note that in models where star-forming galaxies dominate the ionizing UV background, galaxy overdensities should tend to be highly ionized. We therefore consider a scenario in which the damping absorption arises from neutral regions in the foreground of the $z \simeq 6.19$ group.

A neutral island along the line of sight could attenuate Lyα from the $z \simeq 6.19$ group, and would also be expected to produce strong absorption in the spectrum of the quasar. Indeed, the X-Shooter spectrum of Figure 9 shows complete absorption in both Lyα and Lyβ, as well as all higher-order Lyman lines, from the edge of the proximity zone at $z \simeq 6.14$ down to $z \simeq 6.04$. Following Becker et al. (2024), we use the Lyα and Lyβ transmission peaks to calculate the largest mean-density neutral island that could exist within this dark gap. The solid blue line in Figure 9 shows the damping wing profile from a 30.0 h^{-1} cMpc island with its edge located 50.5 h^{-1} cMpc from the quasar, and so $\sim$13 h^{-1} cMpc along the line of sigh from the group at $z \simeq 6.19$. The Lyα attenuation from such an island would only be $\sim$25% at the group redshift, smaller than what we observe. In order to produce a factor of three attenuation, the edge of the island would have to lie $\sim$5 h^{-1} cMpc from the group. Increasing the island length by this amount along the quasar line of sight would violate the observed transmission in the quasar spectrum; however, we note that most of the group is offset from the quasar line of sight by $\sim$3 h^{-1} cMpc. Damping wing attenuation of the group galaxies would therefore be possible if the line-of-sight extent of the island varies across the field.

3.3 A line-of-sight enhancement of Lyα visbility?

In contrast to the $z \simeq 6.19$ group, where we see relatively little emission, we find a high rate of rate of Lyα in two groups at $z \simeq 5.73$ and 5.78. In these groups, four (six) galaxies out of the six show Lyα emission with at least 5σ (3σ) confidence. Although the galaxies at $z \simeq 5.73$ have somewhat fainter UV magnitude and [O III] luminosities, those at $z \sim 5.78$ fall on the brighter end of our sample. Given their spatial coincidence and similarity in redshift, these groups may form a filament-like structure extending radially from $z \sim 5.71$ to $z \sim 5.78$. Such a large ($\sim$21 h^{-1} cMpc) ionized filament could produce a region of locally enhanced ionization, facilitating Lyα transmission.

We note that enhanced transmission of Lyα lines in radially extended ionized filaments has been reported elsewhere. Chen et al. (2024) observed 16 LAEs in three groups at $z \sim 7.2$, $z \sim 7.5$, and $z \sim 7.7$. They suggest that these groups may form an extended structure along the line of sight through which Lyα photons may redshift and escape. Endsley & Stark (2022) detected Lyα emission in nine UV-bright galaxies at $z \sim 6.701$–6.882, suggesting that the LAEs may reside in a large ($R \sim 44$ h^{-1} cMpc) ionized bubble. As part of their work using JADES, MUSE, and FRESCO sources, Witstok et al. (2024) also find that extended structures may enhance the transmission of Lyα from galaxies at $z \sim 5.9$ and 7.3. Our results support

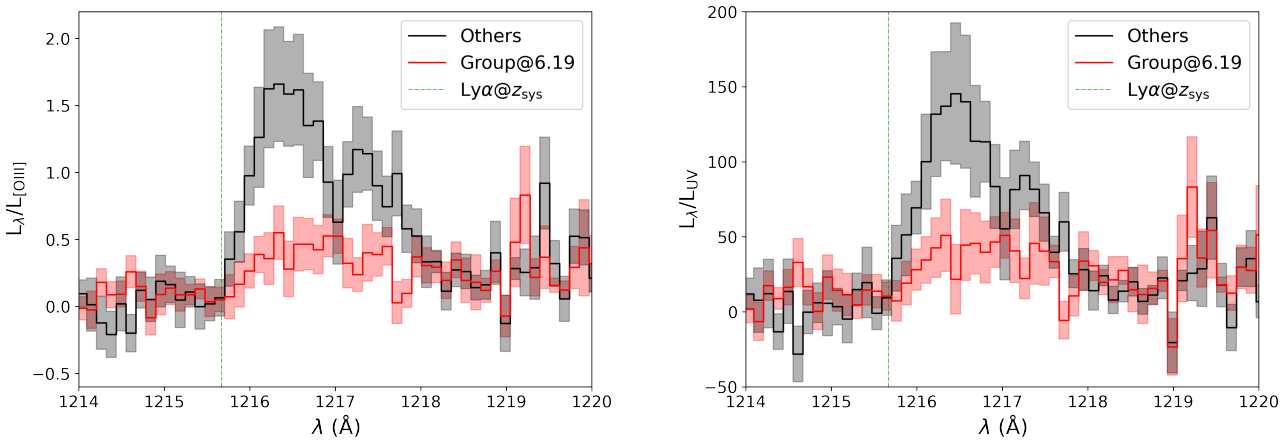

Figure 6. Mean stacked Keck LRIS spectra near Lyα. Red histograms are for the group at $z \simeq 6.19$, while the black histograms are for the remainder of the sample. In the left-hand panel the individual spectra are normalized by their [O III] luminosity prior to stacking, while in the right-hand panel they are normalized by their UV luminosity. Shaded regions show the 1σ variation from bootstrap resampling. The vertical dashed lines correspond to Lyα at the systemic redshift measured from [O III].

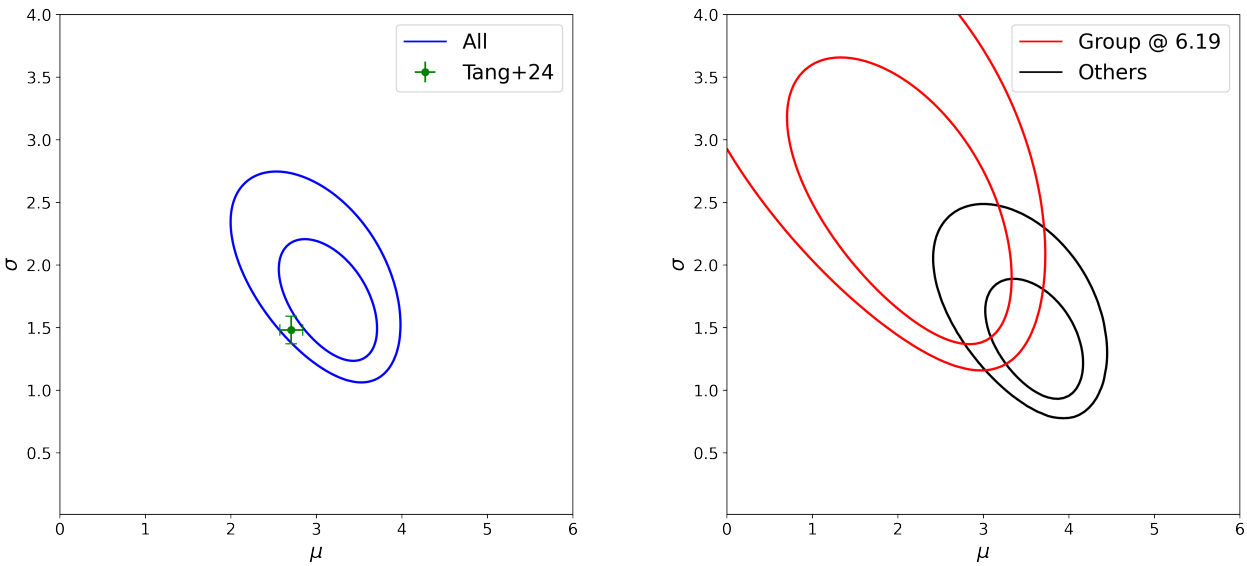

Figure 7. Constraints on a log-normal distribution of Lyα equivalent widths. The contours show the 68% and 95% likelihood bounds for the parameters in Equation 1. The left-hand panel shows the result for the full sample, overplotted with results from (Tang et al. 2024a). The right-hand panel shows results for the group at $z \simeq 6.19$ (red) and the remainder of the sample (black).

the idea that group size and geometry may remain significant factors in the detectability even below redshift six.

3.4 Metal lines and Lyα detection

Finally, we note that our data allow us to take a first look at the potential connection between metal absorbers along the quasar line of sight and Lyα emission from nearby galaxies. There is evidence that the number density of low-ionization metal absorbers declines with decreasing redshift from $z \sim 6$ to 5, an indication that the ionization of circum-galactic metals may at least partly trace the ionization of the IGM near the end of reionization (Becker et al. 2019; Sebastian et al. 2024). If so, then one might expect to see a correlation between metal ionization and the transmission of Lyα from nearby galaxies.

As shown in Figure 4, eight metal absorbers are identified at $z > 5.3$ towards J0100+2802. Three of these systems, at $z_{abs} \approx 5.34$, 6.01, and 6.19 show significant absorption by C IV and are considered high-ionization systems, while the five at $z_{abs} \approx 5.35$, 5.80, 5.95, 6.11, and 6.14 are classified are predominantly low-ionization (Chen et al. 2017; Becker et al. 2019; Cooper et al. 2019; Davies et al. 2023). All of the low-ionization systems except the one at $z_{abs} = 5.35$ show

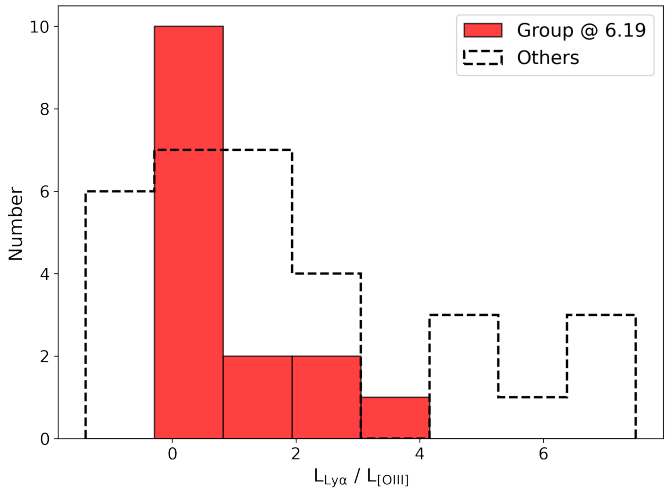

Figure 8. Distribution of the ratio of Lyα and [O III] luminosities. Values for the group at 6.19 are shown in red, while the rest of the sample is shown as a dashed line.

O I absorption and likely trace neutral gas (Becker et al. 2019; Cooper et al. 2019).

Kashino et al. (2023) identified potentially associated [O III] emitters within ±500 km s^{-1} and 300 pkpc of all three high-ionization systems, but only one of the low-ionization systems. We observed two of these (ID 7979 and 6898) associated with the high-ionization systems at redshifts ≃6.01 and 6.19, as well as one (ID 8200) near the low-ionization system at $z \simeq 5.95$. The only one of these we detected in Lyα was ID 6898, which is associated with a high-ionization system, and even in that case the detection was tentative (3σ). Our sample is too small to draw meaningful conclusions between metal absorber properties and galaxy Lyα transmission. We do note, however, that the low-ionization systems are predominantly found in low-density regions, where the local ionizing background may be below average. This is consistent with the idea that low-ionization absorbers tend to trace lower ionization regions (Becker et al. 2019; Doughty & Finlator 2019).

4 SUMMARY AND CONCLUSION

We have used Keck-LRIS to measure Lyα emission from a sample of 46 *JWST* NIRSpec-identified [O III]-emitting galaxies spanning $5.34 \leq z \leq 6.25$. The galaxies are drawn from the EIGER catalog in the field of the $z = 6.33$ quasar J0100+2802 (Kashino et al. 2023). Our primary goal has been to investigate the relationship between environment and Lyα visibility.

In total, we detect 10 galaxies in Lyα emission with at least 5σ confidence. While our overall detection rate is consistent with literature results, we find significant variation between groups. Notably, we find evidence that a large group at $z \simeq 6.19$ may exhibit significantly (factor of ∼3) less transmission than the remainder of the sample. The evidence comes primarily from the ratios of Lyα and [O III] luminosities, although there is tentative evidence that the Lyα equivalent width distribution may also be different. The apparent deficit of Lyα in this group is significant given its size and the fact that it falls within the redshift of the quasar's proximity zone, although most of the group members are significantly offset from the quasar line of sight. We speculate that a foreground neutral island may be scattering Lyα photons from the galaxies in this group. In contrast, we find a high rate of Lyα detections in a pair of closely separated groups at $z \simeq 5.73$ and $z \simeq 5.78$. In this case, the geometric arrangement of an extended structure may be facilitating Lyα transmission.

While it is difficult to draw firm conclusions from this limited sample, our study suggests that environment may play a significant role in the visibility of Lyα emission even as late as $z \sim 6$. If confirmed in larger studies, this could further increase the ability of galaxy Lyα emission to serve as a probe of the end stages of reionization.

ACKNOWLEDGEMENTS

We would like to thank Dr. Jorryt Matthee and the EIGER team for generously sharing the [O III], UV and JWST photometric data for this sample. The authors also would like to thank Dr. Brian Siana for helpful comments. SH and GB were supported by NASA through a grant from the Space Telescope Science Institute grant for *JWST* program GO-4092.

Some of data presented herein were obtained at the W. M. Keck Observatory, which is operated as a scientific partnership among the California Institute of Technology, the University of California and the National Aeronautics and Space Administration. The Observatory was made possible by the generous financial support of the W. M. Keck Foundation. The authors wish to recognize and acknowledge the very significant cultural role and reverence that the summit of Maunakea has always had within the indigenous Hawaiian community.

The authors would like to thank our Keck Observatory Support Astronomers, Percy Gomez and Chien-Hsiu Lee, for their assistance during our observing runs. Special thanks to our Observing Assistant, Arina Rostopchina, for her work.

This work is based in part on observations made with the NASA/ESA/CSA James Webb Space Telescope. These observations are associated with program #1243.

This work made use of the following softwares: numpy (Harris et al. 2020), matplotlib (Hunter 2007), SpectRes (Carnall 2017), scipy (Virtanen et al. 2020), astropy, a community-developed core Python package for Astronomy (Astropy Collaboration et al. 2013, 2018).

DATA AVAILABILITY

The *JWST* data used here are available on the Mikulski Archive for Space Telescopes (`https://mast.stsci.edu/`). Other data will be shared upon reasonable request to the corresponding author.

REFERENCES

Astropy Collaboration et al., 2013, A&A, 558, A33
Astropy Collaboration et al., 2018, AJ, 156, 123
Bañados E., et al., 2018, Nature, 553, 473
Barkana R., Loeb A., 2004, ApJ, 609, 474
Becker G. D., Bolton J. S., Madau P., Pettini M., Ryan-Weber E. V., Venemans B. P., 2015, MNRAS, 447, 3402
Becker G. D., et al., 2019, ApJ, 883, 163
Becker G. D., Bolton J. S., Zhu Y., Hashemi S., 2024, MNRAS, 533, 1525
Bolan P., et al., 2022, MNRAS, 517, 3263
Bosman S. E. I., Fan X., Jiang L., Reed S., Matsuoka Y., Becker G., Haehnelt M., 2018, MNRAS, 479, 1055
Bosman S. E. I., et al., 2022, MNRAS, 514, 55
Carnall A. C., 2017, arXiv e-prints, p. arXiv:1705.05165

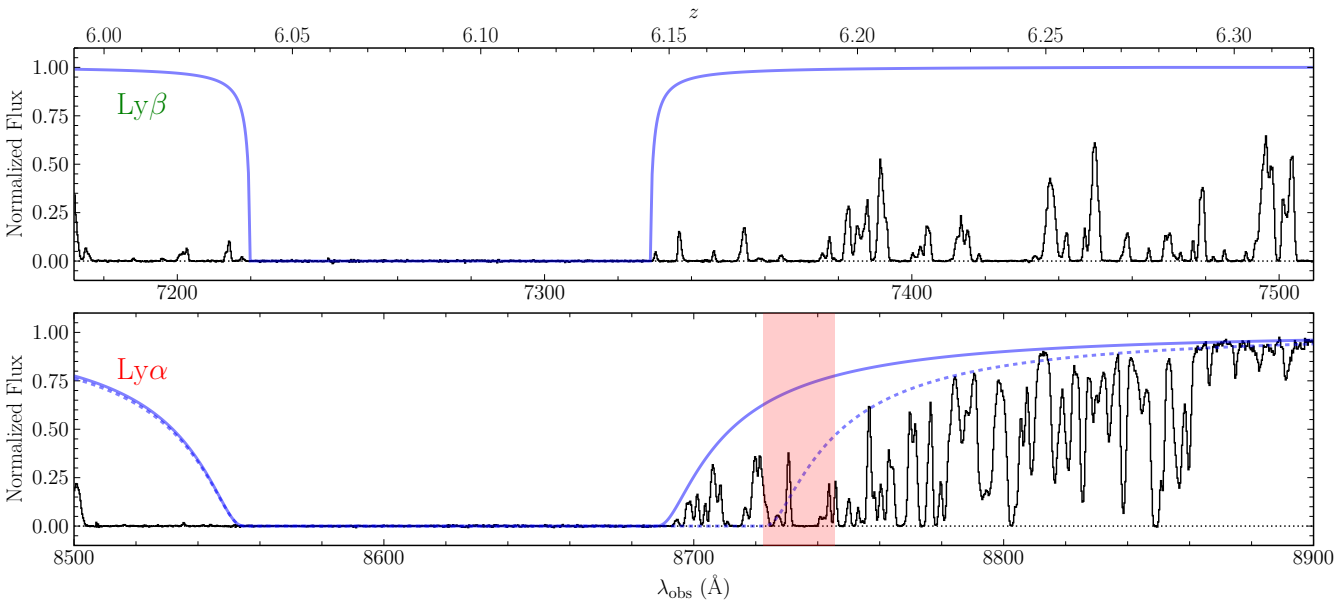

Figure 9. VLT X-Shooter spectrum of J0100+2802 showing transmission in the proximity zone and adjacent absorption trough in Lyα (bottom panel) and Lyβ (top panel). Redshifts corresponding to the observed wavelengths are shown along the top axis. The red shaded region corresponds to the redshift range spanned by the $z \simeq 6.19$ group. Transmission by a plausible neutral island along the quasar line of sight is shown as a blue continuous line. Along the line of sight, the red edge of this island would be ~13 h^{-1} cMpc from the group at $z \simeq 6.19$. At that separation the island would only attenuate Lyα transmission at $z = 6.19$ by ~25%. In contrast, if the red edge of the island is only ~5 h^{-1} cMpc from the group (which itself is transversely offset from the quasar line of sight by ~3 h^{-1} cMpc), then the attenuation would increase to ~60% (dashed line).

Cassata P., et al., 2015, A&A, 573, A24
Chen S.-F. S., et al., 2017, ApJ, 850, 188
Chen Z., Stark D. P., Mason C., Topping M. W., Whitler L., Tang M., Endsley R., Charlot S., 2024, Monthly Notices of the Royal Astronomical Society, 528, 7052
Conaboy L., Bolton J. S., Keating L. C., Haehnelt M. G., Kulkarni G., Puchwein E., 2025, MNRAS, 539, 2790
Cooper T. J., Simcoe R. A., Cooksey K. L., Bordoloi R., Miller D. R., Furesz G., Turner M. L., Bañados E., 2019, ApJ, 882, 77
Curtis-Lake E., et al., 2012, MNRAS, 422, 1425
Davies F. B., et al., 2018, ApJ, 864, 142
Davies R. L., et al., 2023, MNRAS, 521, 289
Dayal P., Ferrara A., 2018, Phys. Rep., 780, 1
De Barros S., et al., 2017, A&A, 608, A123
Dijkstra M., 2014, Publ. Astron. Soc. Australia, 31, e040
Doughty C., Finlator K., 2019, MNRAS, 489, 2755
Eilers A.-C., Davies F. B., Hennawi J. F., 2018, ApJ, 864, 53
Eilers A.-C., et al., 2024, ApJ, 974, 275
Endsley R., Stark D. P., 2022, MNRAS, 511, 6042
Endsley R., Stark D. P., Charlot S., Chevallard J., Robertson B., Bouwens R. J., Stefanon M., 2021, MNRAS, 502, 6044
Endsley R., et al., 2022, MNRAS, 517, 5642
Erb D. K., et al., 2014, ApJ, 795, 33
Fan X., et al., 2006, AJ, 132, 117
Furlanetto S. R., Zaldarriaga M., Hernquist L., 2004, ApJ, 613, 1
Goto H., et al., 2021, ApJ, 923, 229
Greig B., Mesinger A., McGreer I. D., Gallerani S., Haiman Z., 2017, MNRAS, 466, 1814
Greig B., Mesinger A., Bañados E., 2019, MNRAS, 484, 5094
Greig B., Mesinger A., Davies F. B., Wang F., Yang J., Hennawi J. F., 2022, MNRAS, 512, 5390
Greig B., et al., 2024, MNRAS, 530, 3208
Harris C. R., et al., 2020, Nature, 585, 357
Hashimoto T., et al., 2019, PASJ, 71, 71
Hayes M. J., Scarlata C., 2023, ApJ, 954, L14
Heintz K. E., et al., 2024, arXiv e-prints, p. arXiv:2407.06287
Hunter J. D., 2007, Computing in Science and Engineering, 9, 90
Iliev I. T., Mellema G., Pen U. L., Merz H., Shapiro P. R., Alvarez M. A., 2006, MNRAS, 369, 1625
Jin X., et al., 2024, arXiv e-prints, p. arXiv:2410.01318
Kageura Y., et al., 2025, arXiv e-prints, p. arXiv:2501.05834
Kakiichi K., et al., 2025, arXiv e-prints, p. arXiv:2503.07074
Kashino D., Lilly S. J., Matthee J., Eilers A.-C., Mackenzie R., Bordoloi R., Simcoe R. A., 2023, ApJ, 950, 66
Kelson D. D., 2003, PASP, 115, 688
Konno A., et al., 2018, PASJ, 70, S16
Lu T.-Y., et al., 2025, A&A, 697, A69
Mason C. A., et al., 2018a, ApJ, 857, L11
Mason C. A., et al., 2018b, ApJ, 857, L11
Mason C. A., et al., 2019, MNRAS, 485, 3947
Mason C. A., Chen Z., Stark D. P., Lu T.-Y., Topping M., Tang M., 2025, arXiv e-prints, p. arXiv:2501.11702
Matthee J., Sobral D., Gronke M., Pezzulli G., Cantalupo S., Röttgering H., Darvish B., Santos S., 2020, MNRAS, 492, 1778
Matthee J., Mackenzie R., Simcoe R. A., Kashino D., Lilly S. J., Bordoloi R., Eilers A.-C., 2023, ApJ, 950, 67
McGreer I. D., Mesinger A., D'Odorico V., 2015, MNRAS, 447, 499
Meyer R. A., Roberts-Borsani G., Oesch P., Ellis R. S., 2025, arXiv e-prints, p. arXiv:2504.02683
Mortlock D. J., et al., 2011, Nature, 474, 616
Oke J. B., Gunn J. E., 1983, ApJ, 266, 713
Ota K., et al., 2017, ApJ, 844, 85
Ouchi M., et al., 2010, ApJ, 723, 869
Pentericci L., et al., 2014, ApJ, 793, 113
Pentericci L., et al., 2018, A&A, 619, A147
Planck Collaboration et al., 2020, A&A, 641, A6
Roberts-Borsani G., et al., 2023, ApJ, 948, 54
Runnholm A., et al., 2025, ApJ, 984, 95
Santos S., Sobral D., Matthee J., 2016, MNRAS, 463, 1678
Schenker M. A., Stark D. P., Ellis R. S., Robertson B. E., Dunlop J. S., McLure R. J., Kneib J.-P., Richard J., 2012, ApJ, 744, 179
Schenker M. A., Ellis R. S., Konidaris N. P., Stark D. P., 2014, ApJ, 795, 20

Sebastian A. M., et al., 2024, MNRAS, 530, 1829
Simmonds C., et al., 2023, MNRAS, 523, 5468
Spina B., Bosman S. E. I., Davies F. B., Gaikwad P., Zhu Y., 2024, A&A, 688, L26
Stark D. P., Ellis R. S., Ouchi M., 2011, ApJ, 728, L2
Stark D. P., et al., 2017, MNRAS, 464, 469
Tang M., et al., 2023, MNRAS, 526, 1657
Tang M., et al., 2024a, MNRAS, 531, 2701
Tang M., Stark D. P., Ellis R. S., Topping M. W., Mason C., Li Z., Plat A., 2024b, ApJ, 972, 56
Tang M., Stark D. P., Topping M. W., Mason C., Ellis R. S., 2024c, ApJ, 975, 208
Trapp A. C., Furlanetto S. R., Davies F. B., 2023, MNRAS, 524, 5891
Treu T., Schmidt K. B., Trenti M., Bradley L. D., Stiavelli M., 2013, ApJ, 775, L29
Umeda H., Ouchi M., Nakajima K., Harikane Y., Ono Y., Xu Y., Isobe Y., Zhang Y., 2024, ApJ, 971, 124
Umeda H., Ouchi M., Kageura Y., Harikane Y., Nakane M., Thai T. T., Nakajima K., 2025a, arXiv e-prints, p. arXiv:2504.04683
Umeda H., et al., 2025b, ApJS, 277, 37
Virtanen P., et al., 2020, Nature Methods, 17, 261
Wang F., et al., 2020, ApJ, 896, 23
Wang F., et al., 2023, ApJ, 951, L4
Weinberger L. H., Kulkarni G., Haehnelt M. G., Choudhury T. R., Puchwein E., 2018, MNRAS, 479, 2564
Whitler L. R., Mason C. A., Ren K., Dijkstra M., Mesinger A., Pentericci L., Trenti M., Treu T., 2020, MNRAS, 495, 3602
Whitler L., Stark D. P., Endsley R., Chen Z., Mason C., Topping M. W., Charlot S., 2024, Monthly Notices of the Royal Astronomical Society, 529, 855
Willott C. J., Carilli C. L., Wagg J., Wang R., 2015, ApJ, 807, 180
Witstok J., et al., 2024, A&A, 682, A40
Witstok J., et al., 2025, MNRAS, 536, 27
Witten C., et al., 2024, Nature Astronomy, 8, 384
Wyithe J. S. B., Loeb A., 2005, ApJ, 625, 1
Yang J., et al., 2020, ApJ, 897, L14
Zhu Y., et al., 2022, ApJ, 932, 76
Zhu Y., et al., 2024, MNRAS, 533, L49
Ďurovčíková D., et al., 2024, ApJ, 969, 162

APPENDIX A: SOME EXTRA MATERIAL

A1 1D and 2D spectra of our sample

In Figures A1, A2 and A3, we show the 1D and 2D spectra of the remaining of our sample (37 galaxies which are not shown in the main text).

This paper has been typeset from a TEX/LATEX file prepared by the author.

Figure A1. As in Figure 3 but for the remainder of the sample.

Figure A2. Figure A1 continued. In some cases (e.g., object IDs 10020 and 11989), strong and irregular skyline residuals are caused by small irregularities in the slit.

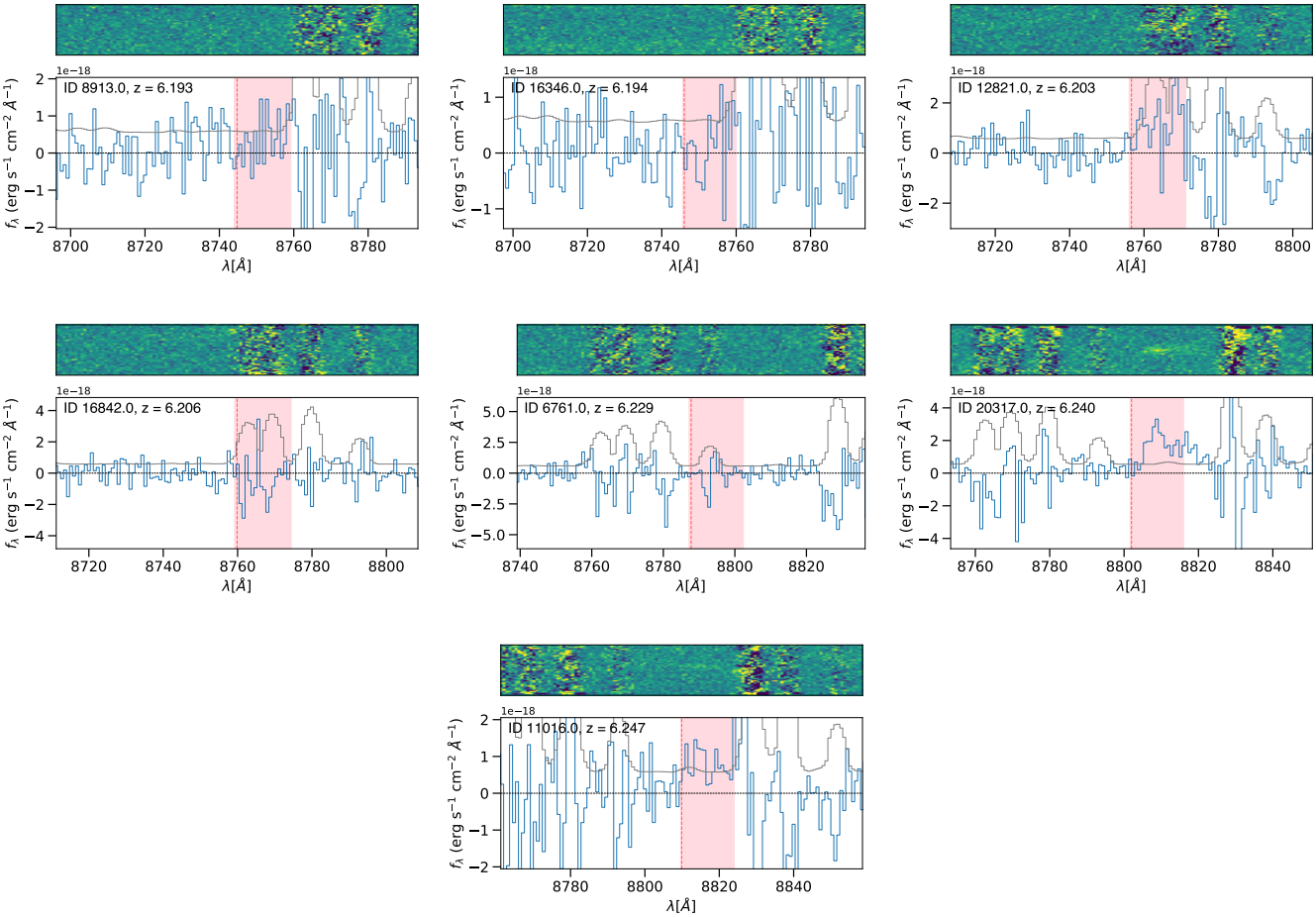

Figure A3. Figure A1 continued